Journal of CO_2 Utilization 23 (2018) 219–225

Contents lists available at ScienceDirect

Journal of CO_2 Utilization

journal homepage: www.elsevier.com/locate/jcou

The anti-sintering catalysts: Fe–Co–Zr polymetallic fibers for CO_2 hydrogenation to $C_2^= – C_4^=$ –rich hydrocarbons

Wenhui Li[a], Anfeng Zhang[a], Xiao Jiang[b], Michael J. Janik[b], Jieshan Qiu[a], Zhongmin Liu[c], Xinwen Guo[a,*], Chunshan Song[a,b,**]

[a] State Key Laboratory of Fine Chemicals, PSU-DUT Joint Center for Energy Research, School of Chemical Engineering, Dalian University of Technology, Dalian 116024, PR China

[b] Clean Fuels & Catalysis Program, PSU-DUT Joint Center for Energy Research, EMS Energy Institute, Departments of Energy and Mineral Engineering and of Chemical Engineering, The Pennsylvania State University, University Park, PA 16802, USA

[c] National Engineering Laboratory for Methanol to Olefins, Dalian National Laboratory for Clean Energy, Dalian Institute of Chemical Physics, Chinese Academy of Sciences, Dalian 116023, PR China

ARTICLE INFO

Keywords:
CO_2 Hydrogenation
Fe-Co-Zr Fibers
K Promotion
$C_2^=$-$C_4^=$-Rich hydrocarbons
Metal sintering

ABSTRACT

Polymetallic fibers of 13Fe2Co/ZrO_2 and 13Fe2Co100Zr were prepared by impregnation and an in situ electrospinning technique. The iron, cobalt and zirconium components in the 13Fe2Co100Zr catalyst are more dispersed than the impregnation one, as indicated by SEM/EDS, TEM, XRD, H_2-TPR and N_2 adsorption techniques. CO_2 conversion increased by a factor of 2 and the selectivity to C_2^+ hydrocarbons increased 15 times on the 13Fe2Co100Zr polymetallic fibers compared with the 13Fe2Co/ZrO_2 supported catalyst. The 0.18 s^{-1} TOF (turnover frequency) of the polymetallic fibers exceeded that of the supported catalyst (0.12 s^{-1}). Potassium addition to the 13Fe2Co100Zr catalyst further improved the selectivity to $C_2^=–C_4^=$, which increased to 27.5% on a 10K13Fe2Co100Zr catalyst. The polymetallic fibers showed stable activity over the reaction period. The activity of the 13Fe2Co/ZrO_2 catalyst, however, decreased rapidly due to metal sintering as observed with TEM and XRD. The in situ electrospinning technique can effectively prevent metal sintering and provide high CO_2 conversion efficiency.

1. Introduction

CO_2 hydrogenation [1,2] is a promising approach to produce hydrocarbon compounds and reduce CO_2 emissions. CO_2 hydrogenation has been studied mainly on traditional metal-supported catalysts, e.g., Fe, Co, Ni and Ru catalysts, that are also used for Fischer–Tropsch synthesis (FTS) [3]. When pure Co, Ni or Ru catalyze CO_2 hydrogenation, a large amount of CH_4 is produced. Co addition to an Fe-based supported catalyst, however, promotes C_2^+ hydrocarbon formation significantly and increases the CO_2 conversion when a low Co/(Co + Fe) ratio is used [4].

Common catalyst supports are oxides, such as Al_2O_3 [5], SiO_2 [6], TiO_2 [7], ZrO_2 [8] and CeO_2 [9]. Among them, Oukaci et al. [10] concluded that Zr played an critical role in moderating Co-support interactions and improving the catalyst stability. Chen et al. [7] tested PtCo bimetallic catalysts supported on TiO_2 and ZrO_2 for CO_2 hydrogenation and found that the PtCo/TiO_2 catalyst converts CO_2 and H_2 into CO, whereas PtCo/ZrO_2 catalyzes the selective formation of CH_4. ZrO_2 provides interesting chemical properties as a support, as it contains both weak acidic sites and basic sites and has multiple stable phases [11]. Furthermore, a higher concentration of active oxygen defects on reduced m-ZrO_2 improves the adsorption and activation of oxygenated species including CO_2 [12,13]. Although Fe-Co metals supported on oxide supports showed good performance for CO_2 conversion, limitations and challenges remain. The poor dispersion of the active metal obtained through traditional impregnation limits activity and stability. Active metal sintering on the support leads to rapid deactivation [14].

A coprecipitation method homogeneously mixes the metal and support precursors and has strengthened the metal-support interaction resulting in a somewhat improved metal dispersion [15]. During the synthesis process, however, uncontrolled sintering of single-metal particles may occur. Electrospinning is a simple and versatile method to transform polymer solutions into nanofibers [16–19]; the long fibers

* Corresponding author.
** Corresponding author at: State Key Laboratory of Fine Chemicals, PSU-DUT Joint Center for Energy Research, School of Chemical Engineering, Dalian University of Technology, Dalian 116024, PR China.
E-mail addresses: guoxw@dlut.edu.cn (X. Guo), csong@psu.edu (C. Song).

http://dx.doi.org/10.1016/j.jcou.2017.07.005
Received 19 May 2017; Received in revised form 25 June 2017; Accepted 4 July 2017
Available online 31 July 2017

can possess larger specific surface areas and higher porosity for reactant adsorption compared with spherical particles. Nanofibers have been widely employed in biomedical research [20], reinforced composites materials [21], electrode materials [18] and catalysis [22]. Compared with traditional supported oxide catalysts, the fiber catalysts can be easily prepared with various polymetallic ratios, and allow for shorter preparation times by avoiding slow crystallization processed and subsequent tabletting processes. More importantly, good dispersion of the different metals in electrospun fibers strengthens the intermetallic synergistic interaction and prevents sintering of single metal particles. Although various nanofibers prepared by electrospinning techniques have been applied for catalysis, the preparation and application of ZrO_2 or Fe-Co-Zr polymetallic fibers as catalysts for CO_2 hydrogenation is a novel approach reported in this study.

Herein, Fe-Co-Zr polymetallic fibers with different Fe/Co molar ratios were prepared through in situ electrospinning, and subsequently tested for CO_2 hydrogenation. A supported $FeCo/ZrO_2$ catalyst was prepared by impregnation onto ZrO_2 fibers to serve as a reference material. The Fe-Co-Zr polymetallic fibers catalysts exhibited superior catalytic performance and stability than the supported $FeCo/ZrO_2$ catalyst.

2. Experimental section

2.1. Fe-Co-Zr polymetallic oxide fiber preparation

Fe-Co-Zr polymetallic fibers were fabricated by an in situ electrospinning method according to a previously reported procedure [20]. Briefly, a solution containing 12 g iron acetylacetone, cobalt acetylacetonate and zirconium acetylacetonate with mass ratios Fe:Co:Zr = 10:5:100, 13:2:100 or 14:1:100; 1.2 g PVP (polyvinyl pyrrolidone); 15.8 g ethanol and 8.4 g acetic acid were mixed by stirring at 60 °C for 30 min. Subsequently, the "sol" was passed through a syringe at a flow rate of 1.0 ml/h with a 22 gauge-blunt needle as the electrospinning tip. The voltage applied for the electrospinning was 22 kV and the distance between needle and collector was 15 cm. The generated fibers were collected onto the aluminum foil and calcined in air at 500 °C for 4 h.

10K13Fe2Co100Zr and 20K13Fe2Co100Zr catalysts were prepared by impregnating the calcined Fe-Co-Zr fibers with an aqueous solution of potassium nitrate to obtain 10 wt% and 20 wt% K loading. The catalysts were obtained after drying at 100 °C for 12 h, followed by calcination in air at 500 °C for 4 h. The catalysts prepared in this work are denoted as (x)K(y)Fe(z)Co(w)Zr, where x, y, z and w represent the mass fraction of the corresponding metals, respectively. The metal contents detected by ICP are listed on Table S1.

2.2. $FeCo/ZrO_2$ catalyst preparation

ZrO_2 nanofiber was first synthesized by electrospinning following the procedure used for Fe-Co-Zr polymetallic fibers. The $13Fe2Co/ZrO_2$ supported catalyst, was prepared by the impregnation method using solutions of iron acetylacetone, cobalt acetylacetonate and the ZrO_2 nanofibers. The fresh catalyst was obtained after drying at 100 °C for 12 h, followed by calcination using a similar procedure as described above.

2.3. Catalytic testing

The catalytic hydrogenation of carbon dioxide was carried out in a pressurized fixed-bed flow reactor (inner diameter 8 mm), with 0.5 g catalyst loaded for each test. Prior to the reaction, the catalyst was pretreated by reduction with pure H_2 at 400 °C overnight. After the reduction, the feed gas was changed to the mixture of carbon dioxide and hydrogen under the reaction conditions of $n(H_2)/n(CO_2) = 3$ (molar ratio), P = 3 MPa, and T = 400 °C. The gaseous hourly space velocity was 7200 ml g^{-1} h^{-1}.

The products were analyzed on-line using a gas chromatograph (FULI GC 97). Carbon monoxide, carbon dioxide and methane were analyzed using a carbon molecular sieve column equipped with a thermal conductivity detector (TCD), while methane and C_2–C_8 hydrocarbons (C_2^+) were analyzed with a flame ionization detector (FID) with a HayeSep Q column. Chromatograms of FID and TCD were correlated through methane, and product selectivity was obtained based on molar amounts of the carbon-containing products.

The conversion of CO_2 and the selectivities of products were calculated as Eqs. (1) and (2):

$$CO_2\ \text{Conversion}(\%) = \frac{n_{CO_2,in} - n_{CO_2,out}}{n_{CO_2,in}} \times 100\% \quad (1)$$

$$S_i(\%) = \frac{m_i n_{i,out}}{n_{CO_2,in} - n_{CO_2,out}} \times 100\% \quad (2)$$

where $n_{co_2,in}$ and $n_{co_2,out}$represent the molar concentration of CO_2 in the feed and effluent, respectively; $n_{i,out}$ represents the molar concentration of product i in the effluent and m_i represents the number of carbon atoms in product i.

2.4. Characterization

XRD patterns of fresh and spent catalysts were collected on a RigakuSmartLab (9) diffractometer with Cu Kα radiation (λ = 1.5406 Å) with a 0.02 step size over the range of 5° and 80°.

Scanning electron microscopy (SEM) images and energy dispersive spectrometer (EDS) maps were obtained on a field emission scanning electron microscopy (NOVA NanoSEM 450) at an accelerating voltage of 10.0 kV. The samples were also studied by high resolution transmission electron microscopy (TEM) and scanning transmission electron microscopy/energy-dispersive X-ray spectroscopy (STEM/EDS) using a JEM-2100F instrument (JEOL Company) with an acceleration voltage of 200 kV. The samples for TEM analysis were prepared by dipping the carbon-coated copper grids into ethanol solutions of the samples and drying at ambient conditions.

The textural properties of the samples were determined by N_2 adsorption on a Quantachrome AUTO-SORB-1-MP sorption analyzer at liquid nitrogen temperature. Prior to the measurements, the samples were degassed at 350 °C for 2 h. The specific surface area was determined by the Brunauer-Emmett-Teller (BET) method. The total pore volume was obtained from the amount of vapor adsorbed at a relative pressure (P/P_0) close to unity, where P and P_0 are the measured and equilibrium pressure, respectively. The pore size distribution was obtained using the adsorption data through the Barrett-Joyner-Halenda (BJH) method.

H_2-temperature programmed reduction (H_2-TPR) measurements were carried out using a ChemBETPulsar TPR/TPD device (Quantachrome, USA) to analyze the reducibility of the calcined catalysts. Prior to reduction, 0.10 g of the calcined sample was charged into the quartz tube and flushed with high purity Ar at 300 °C for 1 h, followed by cooling to room temperature. The TPR program was then initiated by switching to 5 vol% H_2/Ar with a total flow rate of 30 ml min^{-1} and heating to 850 °C at 10 °C min^{-1}.

Dispersion of the oxide particles was characterized by CO titration using the same equipment. Samples were reduced in H_2 at 400 °C for 2 h. After reduction, the gas was changed to high purity Ar for 1 h and then allowed to cool to 30 °C, followed by CO titration. The dispersion was estimated with the assumption of a CO/Fe = 1:2 ratio [23,24].

The iron, cobalt, zirconium and potassium content of the as-prepared samples was measured by ICP-OES (PerkinElmer OPTIMA 2000DV ICP optical emission spectrometer).

Thermogravimetric analysis (TGA) was conducted on a TGA/SDTA851e thermobalance (Mettler Toledo). The TGA data was collected in the range of 30–850 °C in an air flow. The heating rate was

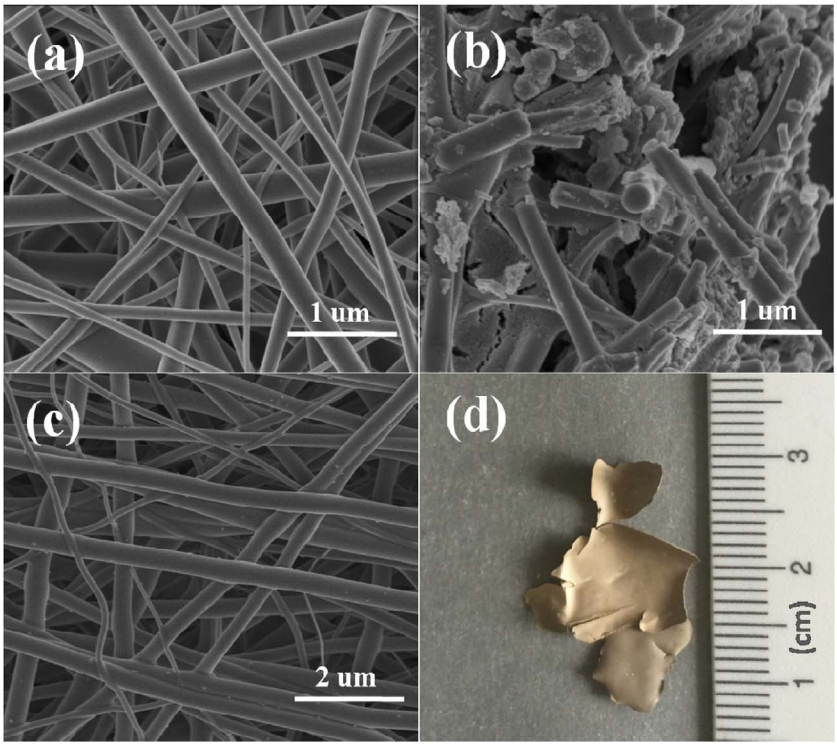

Fig. 1. SEM images of (a) ZrO_2 fibers, (b) 13Fe2Co/ZrO_2 supported catalyst precursor and (c) 13Fe2Co100Zr polymetallic oxide fibers, and (d) photograph of 13Fe2Co100Zr polymetallic oxide fibers.

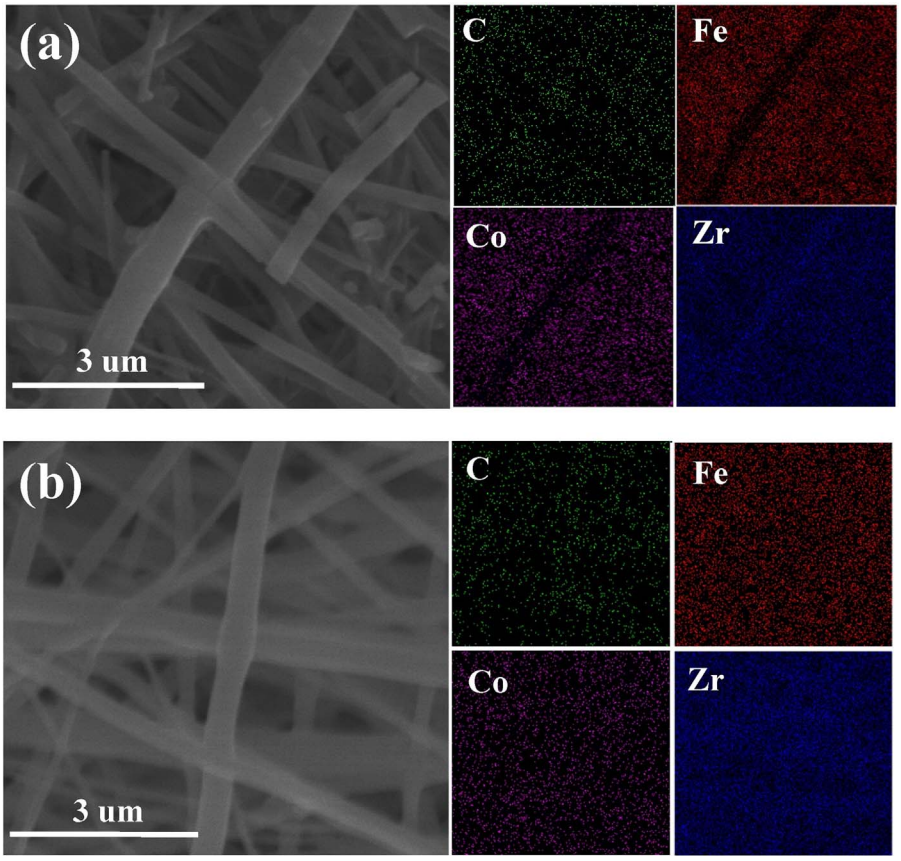

Fig. 2. SEM image and EDS maps of (a)13Fe2Co/ZrO_2 supported catalyst precursors and (b) 13Fe2Co100Zr polymetallic oxide fibers.

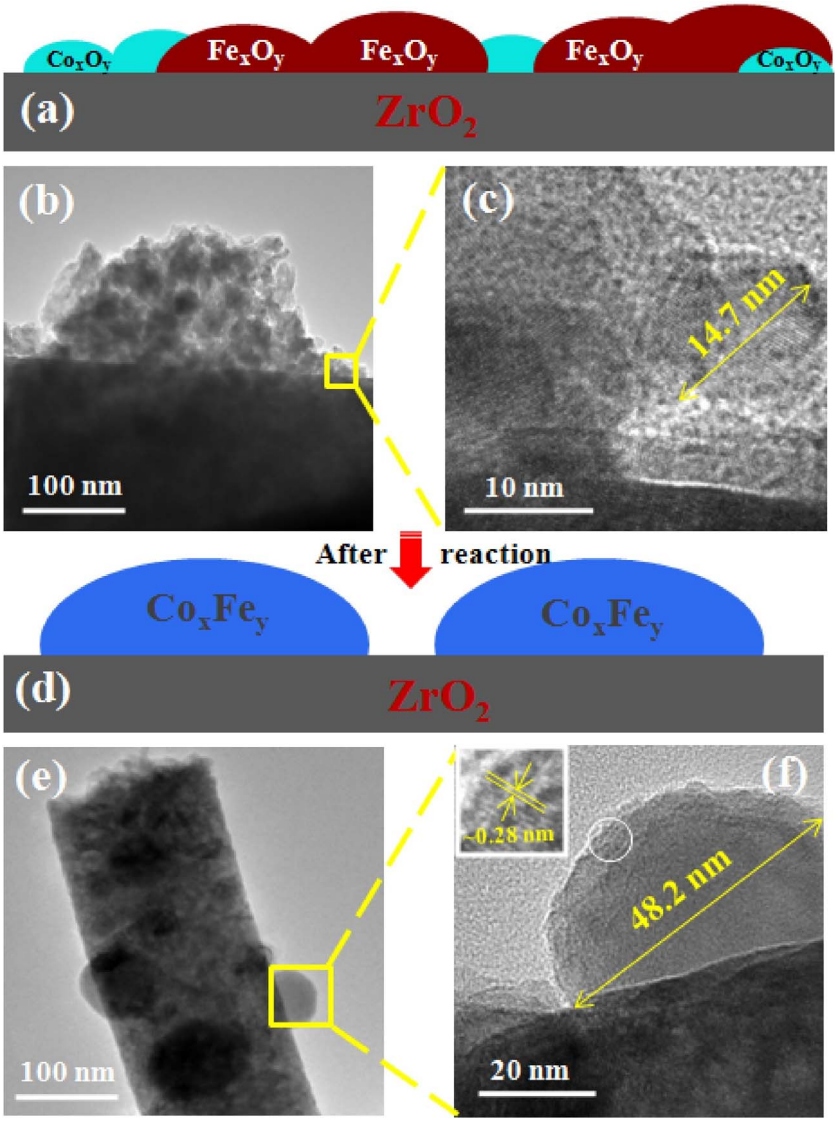

Fig. 3. Schematic illustration of metal distribution and TEM images of 13Fe2Co/ZrO_2 supported catalyst precursor (a–c) and spent catalyst (d–f).

10 °C min^{-1} at a flow rate of 25 ml/min, and the sample weight was between 7 and 10 mg. TG analysis was used to measure the weight change of the catalysts after reaction as well.

3. Results and discussion

3.1. Physicochemical properties

The morphologies of catalysts are shown in Fig. 1. Fig. 1a depicts the SEM image of ZrO_2 fibers. The diameters of ZrO_2 fibers ranged from 100 nm to 300 nm. The SEM image of the FeCo/ZrO_2 catalyst precursor obtained by impregnation is shown in Fig. 1b. The ZrO_2 fibers were clearly broken during the impregnation process. Fig. 1c shows the Fe-Co-Zr polymetallic oxide fibers, with long length and diameters ranging from 100 nm to 400 nm. The oxide fibers are composed of nanoparticles, and the zirconia particle sizes ranged from 10 nm to 20 nm for both catalysts, as will be discussed later (Figs. 3 and 4).

A standard photograph of the Fe-Co-Zr polymetallic oxide fibers is shown in Fig. 1d. The fibers formed a complete film on the aluminum foil that broke partially during the calcination process. Compared to powder catalysts, the flake monolith catalyst can be recycled more easily and has unique advantages for industrial purposes [20].

To investigate the metal dispersion on the fibers, SEM/EDS characterization was carried out (Fig. 2). For the 13Fe2Co/ZrO_2 supported catalyst precursor, an absence of iron and cobalt elements on the ZrO_2 fibers was clear; contrarily, the dispersion of both iron and cobalt is homogeneous in the Fe-Co-Zr polymetallic oxide fibers. The carbon observed from EDS was probably due to the calcination of PVP or the metal precursors. The C content on the 13Fe2Co100Zr polymetallic fibers is 4.7 wt%, which was detected by TG analysis (Fig. S1).

Figs. 3a and 4a illustrate our hypothesized metal dispersion for the two types of catalyst. For the 13Fe2Co/ZrO_2 supported catalyst precursor, the Co and Fe are expected to distribute into separate oxide particles, which might increase the possibility of sintering (Fig. 3a). In contrast, the Fe-Co-Zr polymetallic oxide fibers may benefit from better metal dispersion, and further prevent sintering. The Co and Fe dispersed in proximity to the ZrO_2, but separately from each other, which, in return, helped reduce the possibility of sintering (Fig. 4a). To verify this hypothesis, TEM analysis was conducted over the catalysts precursors; the resulting images are depicted in Figs. 3b–c and 4b–c. In Fig. 3b and c, aggregates composed of Fe and Co oxide nanoparticles are observed on the ZrO_2 fibers, with an average diameter of ca. 15 nm. The Fe and Co oxides nanoparticles successfully dispersed with the ZrO_2 particles for the polymetallic oxide fibers, with an average size of roughly 1–2 nm (see Fig. 4b and c). Clearly, these observations are consistent with our hypothesized structures. The CO adsorption results in Table 2 show that the metal dispersion of 13Fe2Co100Zr polymetallic fibers (e.g., 8%) was higher than that of the 13Fe2Co/ZrO_2

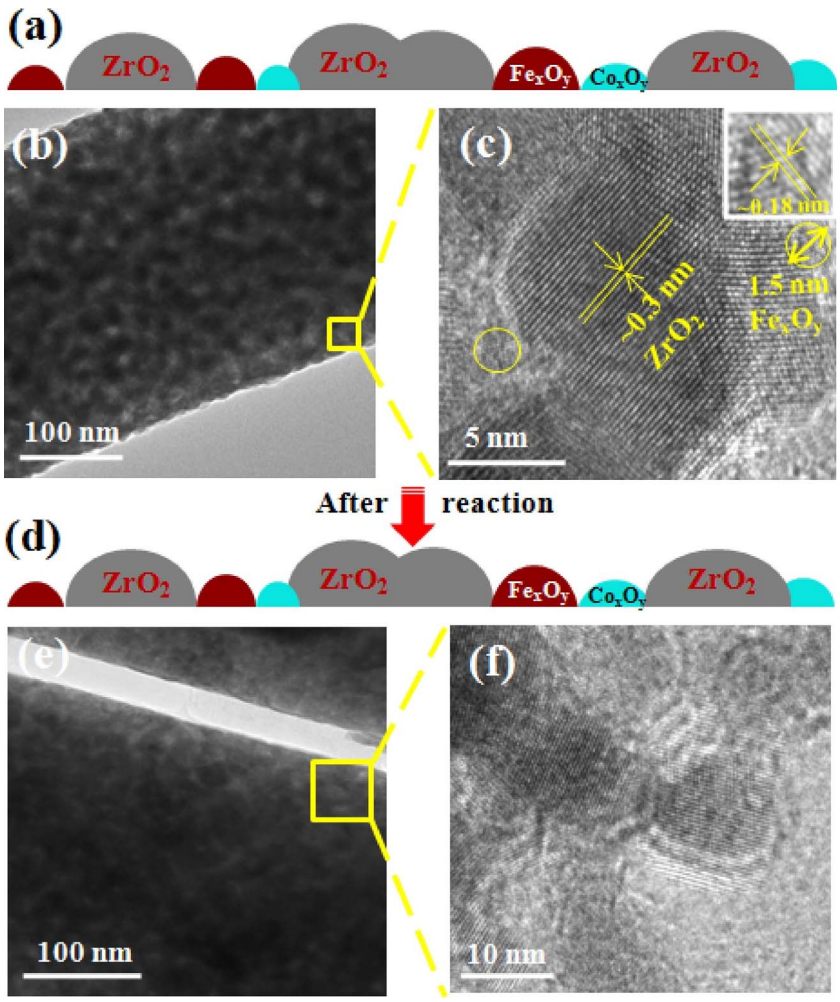

Fig. 4. Schematic illustration of metal distribution and TEM images of 13Fe2Co100Zr polymetallic oxide fibers catalyst (a–c) and spent catalyst (d–f).

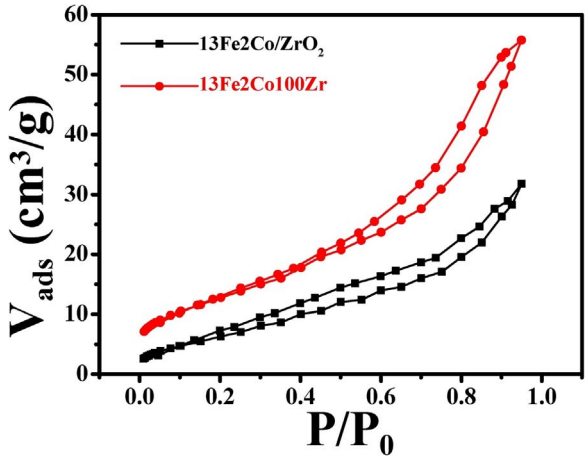

Fig. 5. N_2 adsorption-desorption isotherms of 13Fe2Co/ZrO_2 supported catalyst precursor and 13Fe2Co100Zr polymetallic oxide fibers catalyst.

Table 1
The Physico-chemical properties of 13Fe2Co/ZrO_2 supported catalyst precursor and 13Fe2Co100Zr polymetallic oxide fibers catalyst.

Catalyst	S_{BET} [$m^2\ g^{-1}$]	V_{pore} [$cm^3\ g^{-1}$]
13Fe2Co/ZrO_2	25	0.048
13Fe2Co100Zr	46	0.086

Table 2
Metal dispersion and TOF (turnover frequency) of 13Fe2Co100Zr polymetallic fibers and 13Fe2Co/ZrO_2 supported catalysts.

Catalyst	Metal disp.[a] (%)	TOF[b] (s^{-1})
13Fe2Co100Zr	8	0.18
13Fe2Co/ZrO_2	3	0.12

[a] Metal dispersion was determined by the CO titration analysis.
[b] TOF = (GHSV × 1/4/22.4 × CO_2 Conversion)/(metal molar × reducibility × dispersion)/t.

supported catalyst (e.g., 3%). The CO titration results reconfirmed this observation and corroborate the potential of the electrospun material.

Physical properties of the 13Fe2Co/ZrO_2 supported catalyst precursor and 13Fe2Co100Zr polymetallic oxide fibers were analyzed by N_2 adsorption-desorption isotherms. The isotherms and physical properties of 13Fe2Co/ZrO_2 supported catalyst precursor and 13Fe2Co100Zr polymetallic oxide fibers are shown in Fig. 5 and Table 1. To quantify the adsorption capacity, the specific surface areas of supported catalyst and polymetallic oxide fibers are determined by the BET method, which are 25 m^2/g and 47 m^2/g, respectively. In comparison to the supported catalyst, the higher specific surface area of the polymetallic oxide fibers could lead to a higher metal dispersion with smaller particle sizes. Moreover, the polymetallic oxide fibers exhibited a higher pore volume than the supported catalyst (see Table 1), which might be beneficial for the adsorption and mass transfer of the reactants and products within the porous network. The pore volume (Table 1) calculated by the BJH method are attributed to the

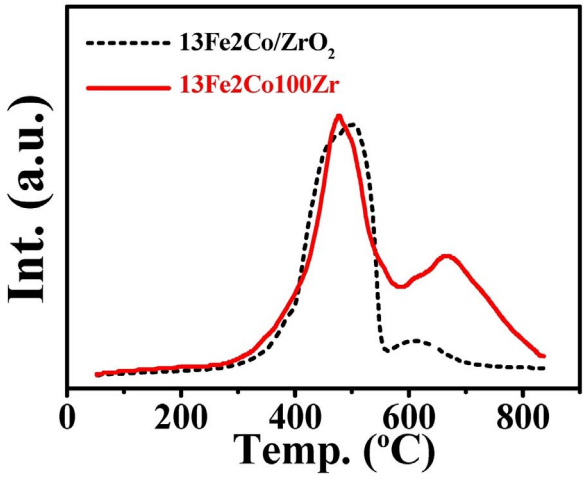

Fig. 6. H_2-TPR profiles of 13Fe2Co/ZrO_2 supported catalyst precursor and 13Fe2Co100Zr polymetallic oxide fibers catalyst.

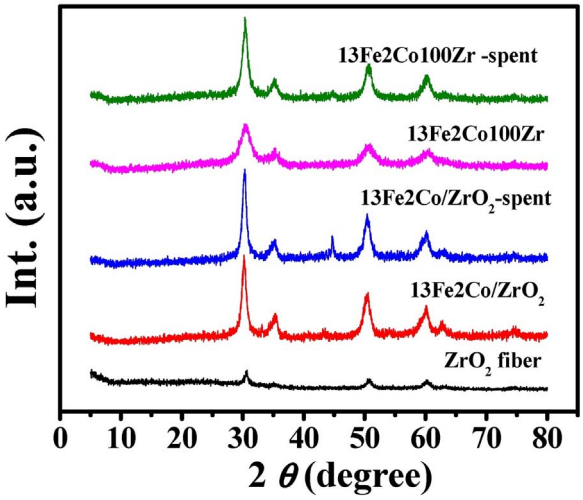

Fig. 8. XRD patterns of fresh and spent catalysts.

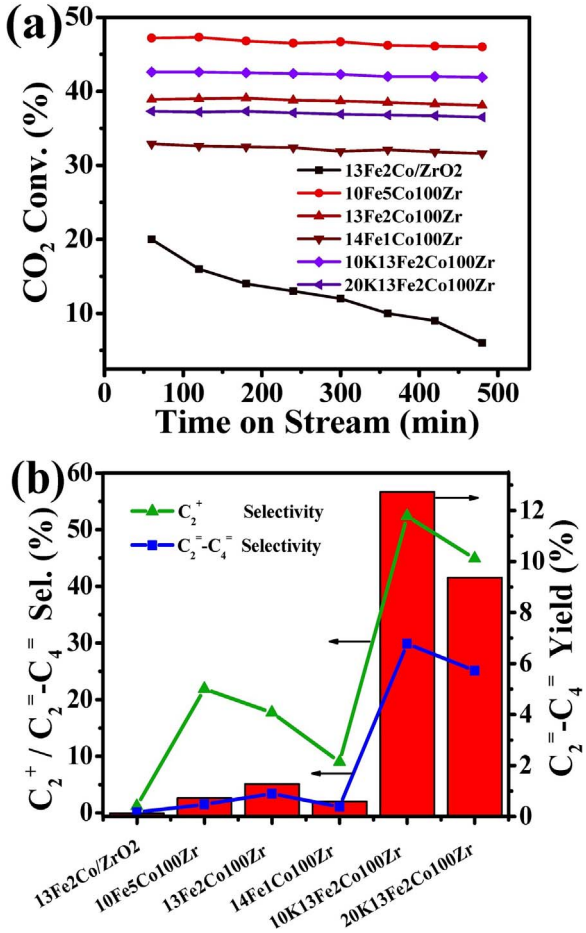

Fig. 7. CO_2 conversion (a) and $C_2^+/C_2^=$–$C_4^=$ selectivity and $C_2^=$–$C_4^=$ yield (b) over different catalysts after 8 h TOS. Reaction conditions: molar ratio of H_2/CO_2 = 3/1, GHSV = 7200 ml g^{-1} h^{-1}, P = 3 MPa, T = 400 °C.

pore formed between particles, which is analyzed from the isotherms.

The reducibility of the two catalysts was also studied by temperature-programmed reduction (TPR), and corresponding profiles are shown in Fig. 6. The reduction of the supported catalyst precursor occurred from 300 °C and exhibited a two-peak pattern with one main reduction peak centered at ca. 500 °C and the other centered at 600 °C. Such profile implied a two-step reduction procedure in the following order: α-Fe_2O_3 → Fe_3O_4 → α-Fe [25]. The profile of the polymetallic oxide fibers exhibited a similar main reduction peak centered at ca. 500 °C, however, the second peak at ca. 600 °C shifted to ca. 680 °C with a long tail on the high-temperature side and became more intense in comparison to the supported catalyst. In addition, the observed ca. 80 °C shift possibly resulted from the strong interaction between the ZrO_2 and surrounding well-dispersed iron/cobalt oxide particles [26,27]. The hydrogen consumption was also estimated by integrating the area under the TPR profile, and the value of 13Fe2Co100Zr polymetallic oxide fibers was 1.25 times that of the supported catalyst precursor, indicating that more metal phases were obtained in the polymetallic oxide fibers. Thus, the TPR analysis demonstrated that the metal oxide particles in the polymetallic oxide fibers had stronger interaction with the ZrO_2 than that on the supported catalyst precursors, due to which the metal dispersion was greatly improved. This observation is consistent with the SEM/EDS and TEM results.

3.2. Catalytic activity

The catalysts were tested in the fixed-bed reactor, and the activities are shown in Fig. 7 (see Table S2 for detailed information). The CO_2 conversion increased by a factor of 2 (Fig. 7a) on the13Fe2Co100Zr catalyst in comparison to the 13Fe2Co/ZrO_2 catalyst at 50 min time on stream. The selectivity of C_2^+ hydrocarbons increased about 15 times (Fig. 8b). Thus, the Fe-Co-Zr polymetallic fibers exhibited superior performance due to the high dispersion of iron and cobalt oxides particles (see Table 2). In addition, 13Fe3Co100Zr polymetallic fibers had a higher conversion efficiency, with a TOF (0.18 s^{-1}) larger than the 13Fe2Co/ZrO_2 supported catalyst (0.12 s^{-1}) (Table 2). Before reaction, the catalysts precursors were reduced on the hydrogen atmosphere and the Fe or Co metal particles were formed to catalyze the reaction; although CO_2 hydrogenation can be catalyzed solely by Fe or Co, the synergetic interaction among Fe, Co and Zr caused higher C_2^+ selectivity and olefin selectivity (Fig. 7b). Furthermore, on the 13Fe2Co/ZrO_2 catalyst, most of the products is carbon monoxide (Table S2). The CO selectivity decreased obviously on the polymetallic fibers compared with the supported catalyst. The strong synergetic interaction among Fe, Co and Zr on the polymetallic fibers can enhance the CO further hydrogenation to hydrocarbons. Strong synergetic interaction promotes the hydrocarbons formation. The greater dispersion of Fe and Co particles in the polymetallic fibers is thought to arise from stronger interaction with ZrO_2. We suggest that such strengthened synergistic interactions among Fe, Co and Zr in the polymetallic fibers is responsible for the observed higher efficiency of CO_2 conversion in comparison to the supported catalyst.

Our prior work concluded that K addition can induce olefin generation [28]. To produce olefin-rich hydrocarbons, we performed additional experiments with K addition. The 13Fe2Co100Zr catalyst showed high $C_2^=$–$C_4^=$ yield and thus was chosen to examine the effect of K on the activity and selectivity for CO_2 hydrogenation. The conversion and selectivity for the K-containing catalyst are depicted in Fig. 7 as well. The CO_2 conversion further increased with 10 wt% K addition, however, it decreased a slightly when the K content was increased to 20 wt%. K addition further improved the selectivity of $C_2^=$–$C_4^=$ to 27.5% for the 10K13Fe2Co100Zr catalyst (Fig. 7b). K serves as an electron donor and changes the H_2 and CO_2 adsorption properties [29], which, thereof, promotes the formation of light olefins. The $C_2^=$–$C_4^=$ olefin yield is also shown in Fig. 7b. The highest $C_2^=$–$C_4^=$ olefin yield (11.6%) was obtained at 10% K addition, which was higher than the previously reported yield of 8.5% [4] The same work, by R. Satthawong et al., also investigated the effect of potassium addition on the light olefin production over Fe17Mn12K8/Al_2O_3. The yield of $C_2^=$–$C_4^=$ olefin over the Fe-Co/K catalyst (8.5%) was higher than that over the classic Fe-Mn-K catalyst (4%) under the same reaction conditions [29]. Moreover, Satthawong et al. also found that there was no olefin formation without K addition for their alumina supported catalysts [4]. We observed a $C_2^=$–$C_4^=$ olefin yield of 1.5% over K-free Fe-CoZr polymetallic fibers in this work. Therefore, it is reasonable to deduce that the ZrO_2 on the polymetallic fibers serve a similar role as the promoter K in Fe-Co/K catalysts, acting as an electron donor to improve the adsorption and activation of CO_2. Further research regarding the adsorption properties of CO_2 and H_2 is of great significance to verify this deduction, and relevant work is undergoing in our lab. In order to clarify the effect of the C (Fig. 2 and Fig. S1) on the hydrocarbons production, 12 mol/L HCl was used to dissolve the metal and metal oxide nanoparticles for 24 h. The obtained material was tested for the CO_2 hydrogenation. There was almost no CO_2 conversion and hydrocarbons production. So, the possibility that the hydrocarbons comes from the C maintained on the catalysts is ruled out.

The activity decreased rapidly on the 13Fe2Co/ZrO_2 catalyst compared with the in situ electrospun catalysts, which can be attributed to rapid sintering of the active metal (see Figs. 3 and 4). Sintering of the 13Fe2Co/ZrO_2 catalyst is observed through XRD (Fig. 8). Seen from Fig. 8, on the catalysts precursors, α-Fe_2O_3 (54.1°) and Co_3O_4 (36.8°) were observed. After reaction, the intensity of the diffraction peak at 44.7° increased on the spent 13Fe2Co/ZrO_2 catalyst, which was associated with metal Fe or the Fe_7Co_3 alloy **(JCPDS: 48-1817).** The sintering on the spent supported catalyst was also confirmed by TEM. Fig. 3e and f shows that the metal oxides or alloy particles (ca. 50 nm) had grown significantly compared to the fresh supported catalyst (ca. 15 nm). Based on the lattice distance shown in Fig. 3f, the sintered particles are likely exposing a Fe_7Co_3 (100) crystal surface, which agrees with the XRD results. Contrarily, the particles on the spent polymetallic fibers exhibited similar sizes as the fresh catalyst (see Fig. 4e and f). Therefore, both XRD and TEM results demonstrated that the in situ electrospinning method had a positive impact on the metal dispersion and prevented the metal from sintering, improving the catalytic stability.

4. Conclusion

FeCoZr polymetallic fibers, prepared by an in situ electrospinning technique, exhibited superior and stable activity for CO_2 hydrogenation. In comparison to the 13Fe2Co/ZrO_2 supported catalyst, the 13Fe2Co100Zr polymetallic fibers exhibited 2-times higher CO_2 conversion and 15-times higher selectivity to C_2^+ hydrocarbons. Detailed characterization results demonstrated the strong synergetic interaction among Fe, Co and Zr in the polymetallic fibers, providing for greater metal dispersion and resistance to sintering. These strong interactions also lead to a higher conversion efficiency and variations in the selectivities of C_2^+ and $C_2^=$–$C_4^=$ olefins. K addition to the 13Fe2Co100Zr catalyst further increased the selectivity for $C_2^=$–$C_4^=$ to 27.5%. This work provides an approach for improving the metal dispersion and maintaining stability of metal catalysts. Also, the versatile in situ electrospinning technique generated a catalyst with good prospects for industrial application of CO_2 hydrogenation to hydrocarbons.

Acknowledgement

This work was financially supported by the National Key Research and Development Program of China (2016YFB0600902-5).

References

[1] J. Graciani, K. Mudiyanselage, F. Xu, A.E. Baber, J. Evans, S.D. Senanayake, D.J. Stacchiola, P. Liu, J. Hrbek, J. Fernandez Sanz, J.A. Rodriguez, Science 345 (2014) 546–550.
[2] W. Wang, S. Wang, X. Ma, J. Gong, Chem. Soc. Rev. 40 (2011) 3703–3727.
[3] R. Satthawong, N. Koizumi, C. Song, P. Prasassarakich, Top. Catal. 57 (2014) 588–594.
[4] R. Satthawong, N. Koizumi, P. Song, J. CO_2 Util. 3-4 (2013) 102–106.
[5] Y. Pan, C. Liu, Q. Ge, J. Catal. 272 (2010) 227–234.
[6] S.A. Gardezi, B. Joseph, Ind. Eng. Chem. Res. 54 (2015) 8080–8092.
[7] S. Kattel, W. Yu, X. Yang, B. Yan, Y. Huang, W. Wan, P. Liu, J. Chen, Angew. Chem. Int. Ed. 55 (2016) 1–7.
[8] M. Al-Dossary, J.L.G. Fierro, Appl. Catal. A: Gen. 499 (2015) 109–117.
[9] F. Wang, C. Li, X. Zhang, M. Wei, D.G. Evans, X. Duan, J. Catal. 329 (2015) 177–186.
[10] R. Oukaci, A.H. Singleton, J.G. Goodwin Jr., Appl. Catal. A: Gen. 186 (1999) 129–144.
[11] K. Tanabe, T. Yamaguchi, Catal. Today 20 (1994) 185–197.
[12] S. Foraita, J.L. Fulton, Z.A. Chase, A. Vjunov, P. Xu, E. Barath, D.M. Camaioni, C. Zhao, J.A. Lercher, Chem.-Eur. J. 21 (2015) 2423–2434.
[13] J. Ye, C. Liu, D. Mei, Q. Ge, ACS Catal. 3 (2013) 1296–1306.
[14] J. Xie, H.M. Torres Galvis, A.C.J. Koeken, A. Kirilin, A.I. Dugulan, M. Ruitenbeek, K.P. de Jong, ACS Catal. 6 (2016) 4017–4024.
[15] J. Liu, B. Sun, J. Hu, Y. Pei, H. Li, M. Qiao, J. Catal. 274 (2010) 287–295.
[16] D. Li, Y. Xia, Adv. Mater. 16 (2004) 1151–1170.
[17] G. Wang, Q. Dong, T. Wu, F. Zhan, M. Zhou, J. Qiu, Carbon 103 (2016) 311–317.
[18] S. Liu, Z. Wang, C. Yu, H.B. Wu, G. Wang, Q. Dong, J. Qiu, A. Eychmuller, X.W. David Lou, Adv. Mater. 25 (2013) 3462–3467.
[19] G. Wang, Q. Dong, Z. Ling, C. Pan, C. Yu, J. Qiu, J. Mater. Chem. 22 (2012) 21819.
[20] H. Wang, Y. Duan, W. Zhong, ACS Appl. Mater. Int. 7 (2015) 26414–26420.
[21] M. Bergshoef, G. Vancso, Adv. Mater. 11 (1999) 1362–1365.
[22] P. Reñones, A. Moya, F. Fresno, L. Collado, J.J. Vilatela, V.A. de la Peña O'Shea, J. CO_2 Util. 15 (2016) 24–31.
[23] N. Lohitharn, J. Goodwin Jr., J. Catal. 260 (2008) 7–16.
[24] N. Lohitharn, J. Goodwin Jr., J. Catal. 257 (2008) 142–151.
[25] X. Gao, J. Shen, Y. Hsia, Y. Chen, J. Chem. Soc. Faraday Trans. 89 (1993) 1079–1084.
[26] Y. Lin, Y. Zhu, X. Pan, X. Bao, Catal. Sci. Technol. 7 (2017) 2813–2818, http://dx.doi.org/10.1039/c7cy00124j.
[27] W. Li, Z. Zhao, F. Ding, X. Guo, G. Wang, ACS Sustain. Chem. Eng. 3 (2015) 3461–3476.
[28] F. Ding, A. Zhang, M. Liu, X. Guo, C. Song, RSC Adv. 4 (2014) 8930–8938.
[29] R. Satthawong, N. Koizumi, C. Song, P. Prasassarakich, Catal. Today 251 (2015) 34–40.